Hydrogen bonding rearrangement by a mitochondrial disease mutation in cytochrome bc_1 perturbs heme b_H redox potential and spin state

Patryk Kuleta[a,1], Jonathan Lasham[b,1], Marcin Sarewicz[a], Iwona Ekiert[a], Vivek Sharma[b,c,2], Robert Ekiert[a,2], and Artur Osyczka[a,2]

[a]Department of Molecular Biophysics, Faculty of Biochemistry, Biophysics and Biotechnology, Jagiellonian University in Kraków, 30-387 Kraków, Poland; [b]Department of Physics, University of Helsinki, FI-00014 Helsinki, Finland; and [c]HiLIFE Institute of Biotechnology, University of Helsinki, FI-00014 Helsinki, Finland

Hemes are common elements of biological redox cofactor chains involved in rapid electron transfer. While the redox properties of hemes and the stability of the spin state are recognized as key determinants of their function, understanding the molecular basis of control of these properties is challenging. Here, benefiting from the effects of one mitochondrial disease–related point mutation in cytochrome b, we identify a dual role of hydrogen bonding (H-bond) to the propionate group of heme b_H of cytochrome bc_1, a common component of energy-conserving systems. We found that replacing conserved glycine with serine in the vicinity of heme b_H caused stabilization of this bond, which not only increased the redox potential of the heme but also induced structural and energetic changes in interactions between Fe ion and axial histidine ligands. The latter led to a reversible spin conversion of the oxidized Fe from 1/2 to 5/2, an effect that potentially reduces the electron transfer rate between the heme and its redox partners. We thus propose that H-bond to the propionate group and heme-protein packing contribute to the fine-tuning of the redox potential of heme and maintaining its proper spin state. A subtle balance is needed between these two contributions: While increasing the H-bond stability raises the heme potential, the extent of increase must be limited to maintain the low spin and diamagnetic form of heme. This principle might apply to other native heme proteins and can be exploited in engineering of artificial heme-containing protein maquettes.

mitochondrial dysfunction | electron paramagnetic resonance | electron transfer | molecular dynamics simulations | density functional theory

Hemes are common redox-active cofactors in biological electron transfer systems. Their major function is to transfer electrons within the cofactor chains or as part of the catalytic sites. The direction and rate of electron transfer are secured by the specific properties of hemes, among which the redox midpoint potential and the spin state are considered to be of crucial importance. Several studies have been carried out to understand how specific molecular elements contribute in adjusting the redox potential values to the levels required for efficient electron transfer rate (1–5). These studies recognized the importance of the heme-iron ligands, the degree of exposure of the heme to the solvent, and specific interactions, including hydrogen bonding, within the amino acids of heme-binding pocket. However, the overall structural complexity of proteins often makes an experimental extraction of individual elements of control extremely challenging, in particular those associated within the hydrogen bonding networks. It is indeed remarkable that the fluctuation of the hydrogen bond network was identified as the factor modulating the efficiency of long-range biological electron transfer (6, 7).

This work focused on exploring the hydrogen bond-related elements of control of the redox properties of one of the hemes of cytochrome b subunit of cytochrome bc_1 (mitochondrial complex III). Cytochrome b is the only subunit of this complex encoded by mitochondrial DNA, thus is a subject of high susceptibility for

spontaneous mutations in comparison to other subunits (encoded by nuclear DNA). Such mutations often lead to systemic disorders, mitochondrial diseases, manifesting in symptoms such as exercise intolerance, myopathies, or neuropathies. On the other hand, their mimic in the bacterial or yeast model systems not only provides insights into the possible molecular basis of the disease but also reveal molecular aspects of protein design (8, 9). With this in mind, we targeted a mutation G34S (human cytochrome b numbering), found in one 52-y-old female patient suffering from exercise intolerance (10). The mutation was present in mitochondria from muscle tissue and caused mild myopathy, lactic acidosis, and defect in mitochondrial complex III activity. The mutated glycine 34 is located on transmembrane helix A of cytochrome b subunit in close distance ($\sim$8 Å) to heme b_H (*SI Appendix*, Fig. S1 *A and B*). This location suggests the possible effect of mutation on the properties of heme cofactor, in particular if one considers that a change of small and nonpolar glycine to a larger and polar serine may affect the local hydrogen bonding environment.

Indeed, the presence of glycine at position 34 was previously noticed as important for heme packing in the cytochrome b subunit (11). Interestingly, the importance of G34 was emphasized by

Significance

To perform their specific electron-transfer relay functions, hemes commonly adopt low spin states with fine-tuned redox potentials. Understanding molecular elements controlling these properties is crucial for the description of natural proteins and engineering redox-active systems. We describe unusual effects of mitochondrial disease-related mutation in cytochrome bc_1, based on which we identify a dual role of hydrogen bonding to the propionate group of heme b_H. We observe that stabilization of the hydrogen bond in mutant enhances the redox potential but destabilizes the low spin state of oxidized heme. This demonstrates a critical role of the hydrogen bonding, and heme-protein interactions in general, to secure a suitable redox potential and spin state, a notion that might be universal for other heme proteins.

the remarkable evolutionary conservation in the equivalents of cytochrome bc_1 complex in distant organisms, such as bacteria, insects, fish, mammals and even plants (12). In a bacterial model (*Rhodobacter sphaeroides* cytochrome bc_1), the equivalent G48 residue was mutated to valine and aspartic acid, both rendering the bacteria photosynthetically incompetent (13). The equivalent of this mutation was also studied in *Saccharomyces cerevisiae* (8). Yeast with G33S (*S. cerevisiae* numbering) mutation were not able to grow aerobically, whereas the isolated bc_1 complex had lower enzymatic activity and disrupted subunit composition (lower level of the iron-sulfur protein assessed by Western blotting and lower cytochrome *b* content, measured optically to 55% of wild type [WT]). The same G33 position was found to be mutated to aspartic acid in a respiratory-deficient yeast (14). Among the 85 tested G33D revertants, 82 were D33G and 3 were D33A, suggesting that only a small amino acid without a charge can be tolerated at this position.

Given the implicated importance of glycine at 34 position of mitochondrial cytochrome *b*, particularly in the context of hydrogen bonding network within the heme-binding pocket, we combined the experimental and computational methods to investigate the effects of introducing serine to the homologous position in purple photosynthetic bacterium *Rhodobacter capsulatus* (mutant G48S). Notably, the bacterial cytochrome *b* shares reasonable sequence similarity with human and yeast mitochondrial cytochrome *b*, close to 57%. We found that G48S perturbs the redox properties of heme b_H and causes structural and hydration changes in the vicinity of heme.

The mutation also severely affects the spectral properties of heme b_H, which are best explained by a model assuming a reversible change from low to high spin state when the heme is oxidized. The latter comes as a rather unusual and unexpected molecular effect, considering all so-far reported effects of disease-related mitochondrial mutations (8, 9, 15). At the same time, it offers interesting insights into the role of hydrogen bonding and protein packing in maintaining the low spin state of the oxidized heme fostering electron-transfer relay function.

Results

The Spectroscopic Properties of G48S Mutant.

The unusual electron paramagnetic resonance spectra of hemes b in G48S mutant. As a first step of investigation of the molecular effects of mitochondrial mutation equivalent in *R. capsulatus*, the basic characterization of the mutant was performed. Bacteria with G48S mutation on cytochrome *b* in comparison to WT exhibited only slightly slower growth under cytochrome bc_1-dependent photosynthetic conditions, suggesting that mutated complex is functional (*SI Appendix*, Fig. S2). However, several attempts of G48S purification resulted in varying stoichiometry of the complex subunits indicating its low stability in solution. Therefore, all of the further analyses were carried out using membrane chromatophores. The optical absorption spectra of hemes and electron paramagnetic resonance (EPR) spectra of [2Fe-2S] cluster did not reveal significant changes in G48S chromatophores in comparison to WT (*SI Appendix*, Fig. S3). Also, the light-activated kinetics (measured under conditions with quinone [Q] pool half-reduced) did not reveal any major difference in rates of heme b_H reduction from quinol oxidation at Q_o site, with only heme b_H reoxidaton impaired in G48S in comparison to WT (Table 1).

However, the unusual behavior of hemes in G48S was revealed by continuous wave (CW) EPR spectroscopy at low temperature. Under typical conditions, the WT sample fully oxidized with ferricyanide exhibits the g = 3.41 transition, corresponding to oxidized low spin heme b_H (16). This signal is also present in the ascorbate-reduced sample (Fig. 1*A*, black), indicating that the heme remains oxidized, which is consistent with the well-described low redox midpoint potential (E_{m7}) of this heme (~50 mV) (17). In G48S mutant, this EPR transition was not present neither in a sample fully oxidized (see top black spectrum in Fig. 2*B*, *Right*) nor reduced with ascorbate (Fig. 1*B*, black). At the same time, the

transition corresponding to oxidized heme b_L was observed in G48S with the same value g = 3.78 as for WT sample (Fig. 1). In previous studies, the lack of g = 3.41 was observed when the bis-His ligation pattern of heme b_H was changed by mutation (18). Thus, the lack of g = 3.41 in G48S immediately suggests that this mutation also might introduce structural changes affecting the heme-ligand interactions.

Interestingly, addition of antimycin (the Q_i site-specific inhibitor) to the ascorbate-reduced sample resulted in the appearance of resonance transition g = 3.40 reflecting the oxidized heme b_H (Fig. 1*B*, red). This phenomenon was not observed for the fully oxidized sample inhibited with antimycin (Fig. 1*C*, red); to observe the g = 3.40 transition, the G48S sample must have been reduced with ascorbate prior to the addition of antimycin (Fig. 1*C*, green). It is of note that the g value (g = 3.40) of G48S corresponded to the g value of heme b_H in WT in the absence of antimycin (in WT, addition of antimycin results in the shift of its EPR g transition from 3.41 to 3.45).

These results indicate that in G48S mutant, the redox properties of heme b_H are significantly changed in comparison to WT. The most straightforward explanation for the lack of g = 3.41 EPR transition in the G48S sample is an increase in the E_m of heme b_H, which would have to be large enough to render this heme fully reduced in the presence of ascorbate (i.e., the E_m of the heme b_H would have to be in the range of 200 mV or more). This prompted us to look more closely into the redox properties of this heme.

Influence of G48S mutation on the redox properties of heme b_H observed by optical spectroscopy. The redox equilibrium between hemes *b* and the Q pool was monitored by light-induced electron transfer under the conditions favoring electron transfer from quinol occupying Q_i site to oxidized heme b_H. This reaction can be observed with the Q_o site-specific inhibitor (in this work, myxothiazol) when the reducing power of the Q pool is increased (by increasing pH) and the Q pool is oxidized before the light activation (19). The rate of heme b_H reduction under these conditions for G48S mutant is approximately 10-fold lower than WT (Table 1), whereas the amplitude is two times higher (Fig. 1 *D* and *E*, blue) approaching the level of heme b_H reduction in the absence of inhibitors (Fig. 1 *D* and *E*, black). The observed increase in the amplitude of heme b_H reduction in G48S could be a result of either an increase in the E_m of the heme or a modified interaction of the heme with the redox-active occupant of the Q_i site, which would lead to an "apparent" increase of E_m of the heme.

To distinguish between these two possibilities, the optical redox potentiometric titrations of the G48S mutant in the absence and presence of antimycin were analyzed in reference to WT. At pH 7, hemes *b* in WT without inhibitors titrate with E_m values of +128 mV, +60 mV, and −124 mV, corresponding to heme b_{HH} (a fraction of heme b_H with higher E_m), heme b_{HL} (a fraction of heme b_H with lower E_m), and heme b_L, respectively (Fig. 1*F*, black). The presence of two forms of heme b_H (b_{HH} and b_{HL}) is well established and interpreted as an indication of interaction of the heme with the redox-active occupant of the Q_i site (20, 21). When this interaction is prevented in the presence of antimycin, heme b_H titrates as one component with E_{m7} of +60 mV (Fig. 1*F*, red).

G48S without inhibitors titrates with the three components having E_m values of +148 mV, +21 mV, and −136 mV (Fig. 1*G*, black), which correspond to hemes b_{HH}, b_{HL}, and b_L of WT, respectively. The main difference is a considerably larger fraction of the high-potential heme b_{HH} (E_m +148 mV), which in G48S accounts for about 50% of total b-type hemes, whereas it only accounts for 30% in WT. In the presence of antimycin, heme b_H in G48S titrates as one component with E_m of +73 mV (Fig. 1*G*, red), which closely resemble titrations of this heme in WT. The larger amplitude of heme b_{HH} in G48S in the absence of inhibitors and the lack of significant changes in E_m of this heme in the presence of antimycin indicate that the apparent increase in E_m

Table 1. Selected properties of G48S mutant in comparison to WT

| | Phenotype* | Light-induced heme b[†] | | Q_i reverse | E_{m7} of hemes | | | E_{m7} of hemes | |
| | | Reduction, s^{-1} | Reoxidation, s^{-1} | Reaction, s^{-1}[‡] | Spectrophotometry | | | EPR | |
					b_{HH}, mV	b_{HL}, mV	b_L, mV	b_{HL}, mV	b_L, mV
WT	+++		180	400	128	60	−124	nd§	nd
+ ant		1,050			—	60	−120	51	−102
G48S	++		50	35	148	21	−136	—	—
+ ant		980			—	73	−112	62	−105

*++ indicates photoheterotrophic growth slower than WT.
†Measured at pH 7.0 and E_h = 100 mV (Q pool half-reduced).
‡Measured at pH 9.0 and E_h = 250 mV (Q pool oxidized).
§nd, not determined.

of heme b_H in G48S is in part related to modified interaction of this heme with surroundings and also in part with the redox-active occupant of the Q_i site.

Intriguingly, the magnitude of this increase is not large enough to explain the lack of g = 3.40 transition in the ascorbate-reduced sample in the absence of antimycin (Fig. 1B, black). To solve this discrepancy, we performed EPR redox titrations of hemes b in G48S and WT. These titrations monitor disappearance/appearance of oxidized low spin hemes and thus complement the optical titrations, which monitor disappearance/appearance of the reduced hemes. We thus expected that combining both types of titrations would help us understand the properties of heme b_H in G48S.

Indication of heme b_H spin state conversion by G48S mutation from EPR measurements. The EPR redox titrations were carried out in a wide range of magnetic induction to observe changes of all possible resonance transitions upon changing the redox state of the sample. The reductive titration of fully oxidized sample did not reveal any signal of low spin paramagnetic centers (highly axial low spin [HALS] type) that could be assigned as heme b_H (Fig. 2, step 1). Moreover, addition of antimycin at ambient redox potential (E_h) ~40 mV (which is below the E_m value of heme b_H in WT) did not change the EPR spectra of hemes (Fig. 2, step 2). However, the subsequent oxidative titration with ferricyanide (i.e., after addition of antimycin) resulted in the appearance of resonance transition g = 3.40, the amplitude of which increased with the increase of E_h reaching a maximum at around 200 mV (Fig. 2, step 3). The E_m of this transition was calculated to be +62 mV at pH 7.0 (Fig. 2C, Right), which is remarkably similar to the E_m of heme b_H described for WT (17). Given this similarity and the position of g, this transition was assigned as the low spin heme b_H (22, 23).

Interestingly, along with the changes seen in g = 3.40 transition, the unusual and absent in WT changes of resonance
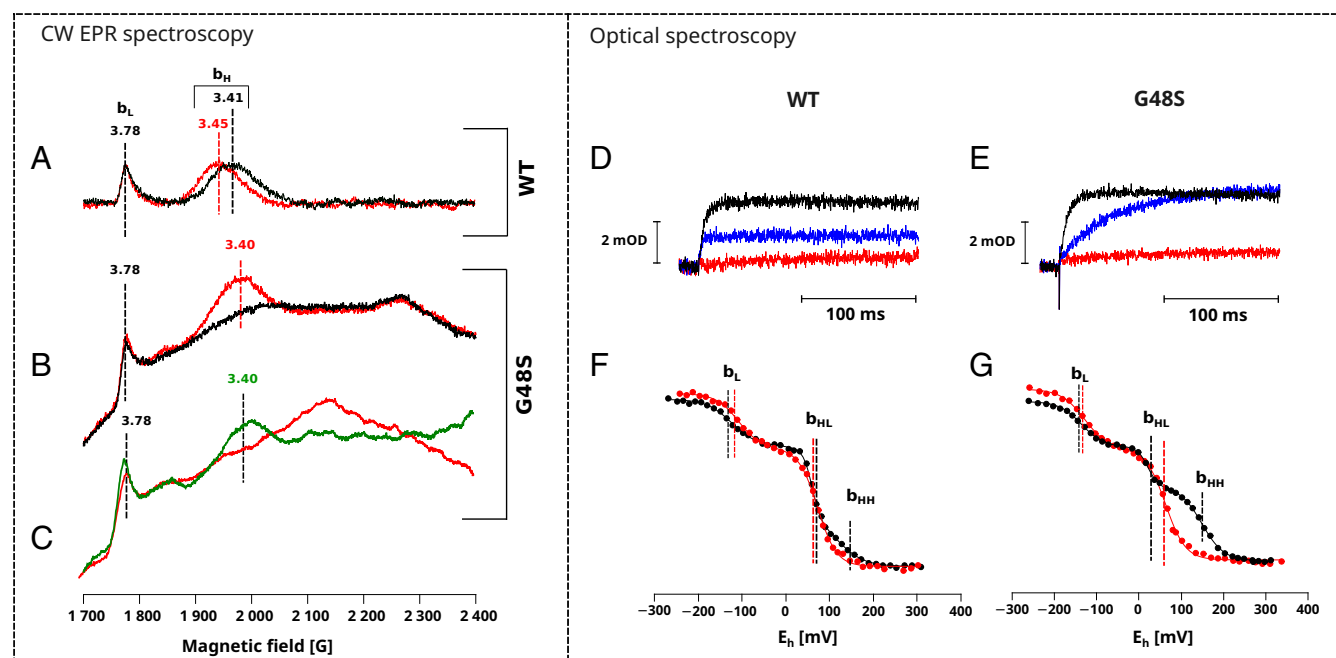
Fig. 1. Comparison of selected spectroscopic properties of WT and G48S in chromatophores. CW EPR spectra of hemes: (A) WT sample reduced with ascorbate (black) and with subsequent inhibition by antimycin (red); (B) G48S sample reduced with ascorbate (black) and subsequent inhibition by antimycin (red); and (C) G48S oxidized sample inhibited with antimycin (red) and with subsequent reduction by ascorbate (green). Optical spectroscopy (D and E): light-induced redox kinetics of hemes b_H for WT and G48S, respectively. Reduction of heme b_H through reverse electron transfer at the Q_i site followed at 560 to 570 nm. Traces were recorded without inhibitors (black), with myxothiazol (blue), and with myxothiazol and antimycin (red) at pH 9 and ambient potential of 250 mV; (F and G) optical redox titration of b-type hemes measured for WT and G48S chromatophores respectively at pH 7.0 for samples without inhibitors (black) and with antimycin (red).
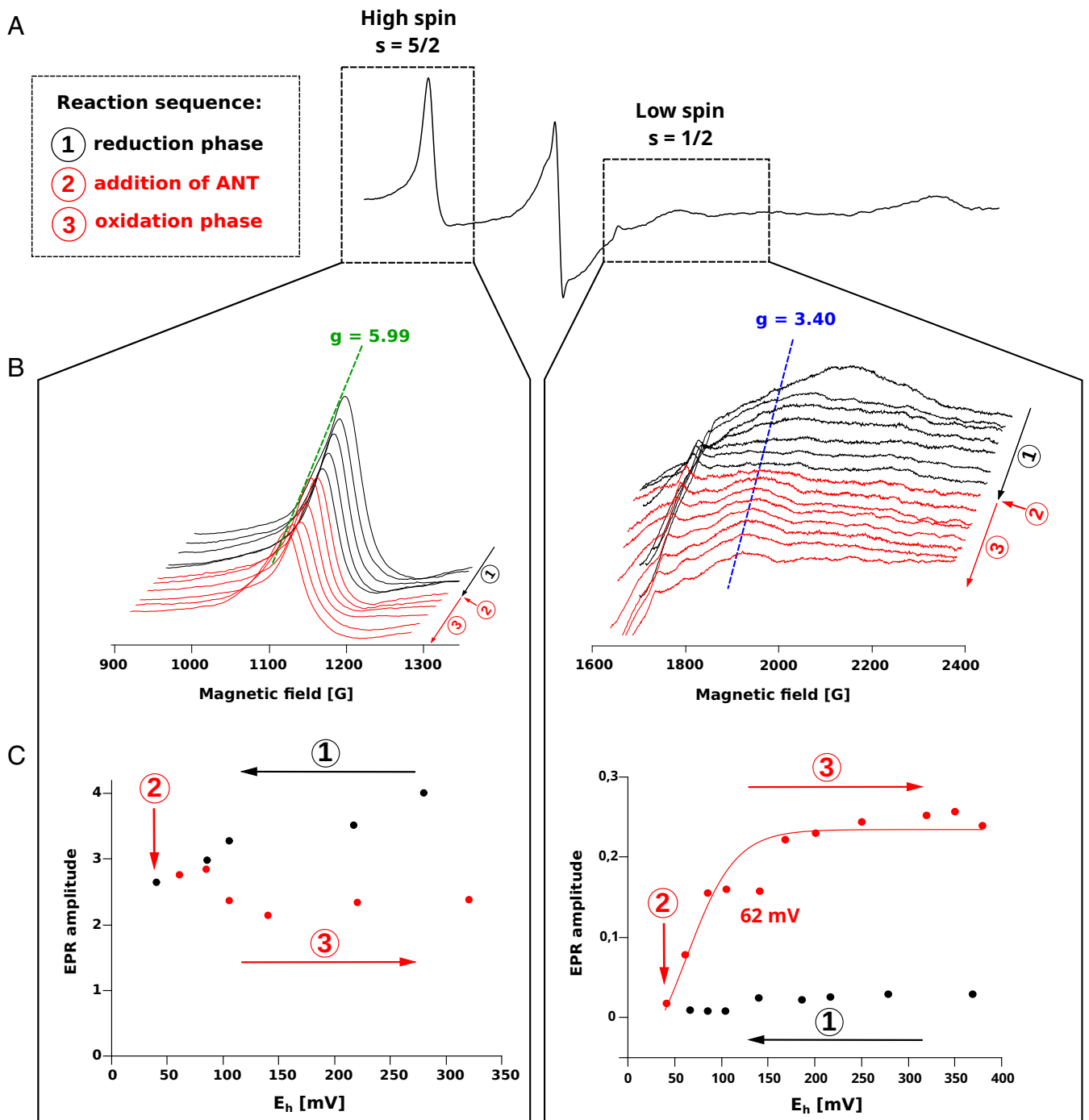
Fig. 2. CW EPR spectral changes in G48S chromatophores upon reductive and oxidative redox titrations. Reaction sequence: 1) reductive titration from fully oxidized sample to value below the E_{m7} of WT heme b_H; 2) addition of antimycin (ANT); and 3) oxidative titration rising the potential to the initial value. (*A*) Example of CW EPR spectrum of G48S with marked regions of high and low spin resonance transition of hemes. (*B*) Parts of CW EPR spectra showing transitions g = 5.99 (*Left*) and g = 3.40 (*Right*) recorded at various redox potentials. (*C*) The dependence of CW EPR signal amplitude of high spin (*Left*) and low spin (*Right*) on the ambient redox potential (E_h) obtained from the spectra shown in *B*; the color of dots indicates reductive and oxidative potentiometric titration (black and red, respectively).

transition g = 5.99 were also observed. During the reductive titration, the amplitude of this transition decreased significantly (Fig. 2*B*, green dashed line) and did not rise to the initial value during the oxidative titration (Fig. 2*C*, *Left*). Considering that g = 5.99 transition is characteristic for high spin oxidized hemes (23, 24), it suggests that in contrast to WT in mutant, there is a

fraction of high spin hemes. During the reductive titration of G48S, the low spin heme b_H signal is not observed but appears during the oxidative titration phase. It is thus clear that the g = 3.40 transition appears at the expense of g = 5.99. To explain all these observations, we conclude that the oxidized heme b_H in the G48S is high spin (no g = 3.40 transition) and upon reduction

Kuleta et al.
Hydrogen bonding rearrangement by a mitochondrial disease mutation in cytochrome
bc_1 perturbs heme b_H redox potential and spin state

undergoes conversion to low spin (no g = 3.40 transition but optical maximum at 560 nm).

The interactions of G48S at atomic level. All experimental results indicated some prominent changes of spectroscopic and redox properties caused by G48S mutation. However, their molecular bases were difficult to explain. Thus, we engaged computational methods to study the possible structural changes and interactions of mutated residue with local protein environment, especially with heme b_H. To investigate the effects of mutation at an atomic level, classical atomistic molecular dynamics (MD) simulations were performed on models built from crystal structures of *R. capsulatus* and *S. cerevisiae* cytochrome bc_1 (Protein Data Bank [PDB] IDs 1ZRT and 3CX5, respectively) (25, 26). Additionally, in order to shed light on the redox behavior of heme b_H, density functional theory (DFT) calculations on WT and mutant cluster models were performed.
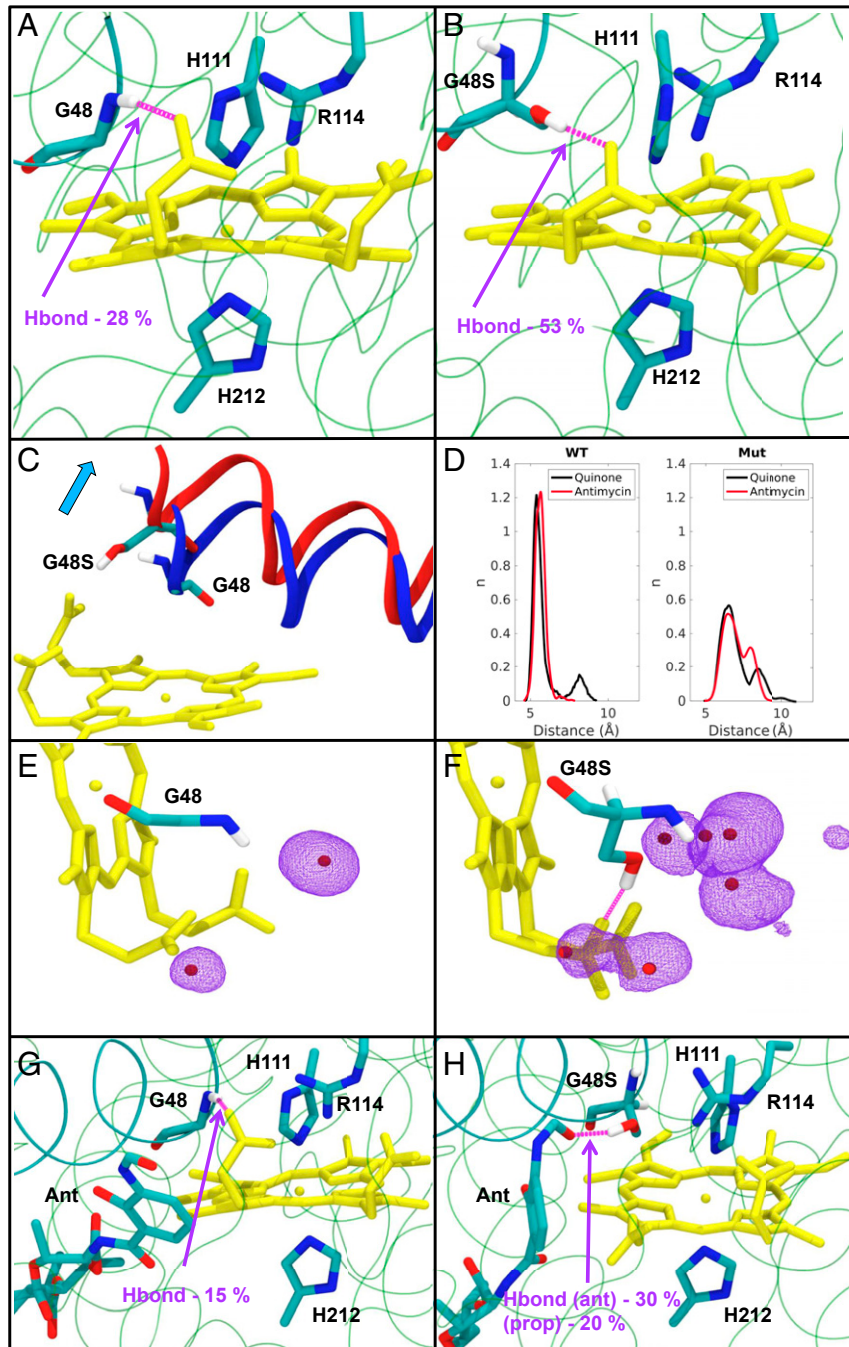
Fig. 3. Snapshots from MD simulation of bacterial cytochrome bc_1 showing H-bonding between propionate and Gly backbone in WT (*A*) and Ser sidechain in mutant (*B*). The hydrogen bond occupancy is labeled. (*C* and *D*) The structural rearrangement of transmembrane helix A in WT (blue) and G48S (red). The two conformations of Gly and Ser ("near" and "far") are shown as a histogram (normalized such that area under the curve is equal to one) of distance between backbone Cα of Gly/Ser and Fe of heme b_H. (*E* and *F*) Water occupancy near the propionate region in WT and G48S mutant, respectively. Water occupancy is shown as dotted surface (20% occupancy, data from all simulation trajectories). (*G*) Simulation snapshot showing H-bond between propionate and Gly backbone in WT with antimycin (Ant) bound the at Q_i site. (*H*) Simulation snapshot with H-bonding between G48S sidechain and antimycin is shown, together with the H-bond occupancies.

Kuleta et al.
Hydrogen bonding rearrangement by a mitochondrial disease mutation in cytochrome bc_1 perturbs heme b_H redox potential and spin state

PNAS | 5 of 10
https://doi.org/10.1073/pnas.2026169118

Structural rearrangement and altered hydrogen bonding caused by G48S.
The results of MD simulations reveal a clear local difference
between the WT and G48S mutant. In bacterial WT complex
simulations, the backbone of Gly48 (-NH) makes an H-bond
with the propionate group of heme b_H with 28% ± 4% occu-
pancy of all simulated trajectories (Fig. 3*A*). However, in mutant,
structural rearrangement takes place, causing H-bond formation
between heme b_H propionate and Ser48 sidechain (-OH) instead
of the protein backbone. This relatively stable H-bond occurs
rapidly (<1 ns) with an occupancy of 53% ± 6% over all G48S
simulation trajectories (Fig. 3*B*). The same scenario is observed
in MD simulations of mitochondrial cytochrome bc_1, where even
more drastic difference occurs in H-bond occupancies of WT
and mutant. While the serine sidechain-based H-bond to pro-
pionate is highly stable for 79% ± 1% of total simulation time,
the glycine backbone forms a weaker H-bond with ca. 13% ± 2%
occupancy (*SI Appendix*, Fig. S4 *A* and *B*). Interestingly, presence
of a bulkier serine instead of glycine also causes structural per-
turbation, which is observed as slight bending of the transmem-
brane A helix (Fig. 3*C*). In addition, two different conformational
arrangements are observed in simulations of mutant bacterial cy-
tochrome bc_1. In one case, Ser48 resides next to the His111 ligand
of heme b_H ("near" arrangement, ca. 6 Å distance between Ser Cα
and Fe atoms), whereas in another case it shifts further away
("far" arrangement, ~8.5 Å distance between Ser Cα and Fe
atoms), with the H-bond to propionate still retained (Fig. 3*D*). In
contrast, the more tightly packed "near" arrangement is found to
be highly stable in WT Gly case (Fig. 3*D*). This tight packing
partly restricts the conformational freedom of the His111 ligand
(*SI Appendix*, Fig. S4*C*). We also find that due to the larger
structural variability of polar side chain of serine as in "far" ar-
rangement, more space is created, which also results in a higher
level of hydration near the heme propionate group in mutant in
comparison to WT enzyme (Fig. 3 *E* and *F*). Clearly, mutation of
Gly to Ser changes the dynamics and polarity of the region,
which may explain the spectroscopic differences observed be-
tween WT and mutant.

The results from DFT calculations on bacterial model systems
show that when Ser sidechain is H-bonding to the propionate
group, as opposed to Gly backbone, it enhances the electron af-
finity of heme b_H by ~0.13 eV. This effect is observed in all three
different DFT functionals used (0.11 ± 0.05 eV in B3LYP, 0.15 ±
0.06 eV in TPSS, and 0.14 ± 0.07 in TPSSh). The increase in
electron affinity is also seen based on DFT calculations performed
on high-resolution structure of mitochondrial bc_1 complex, albeit
the effect is relatively milder (30 meV to 40 meV across the three
density functionals utilized). Overall, the data clearly indicate that
even the subtle change in hydrogen bonding environment affects
the heme b_H redox properties.

The influence of antimycin on H-bonding arrangement in G48S mutant. In
order to study the effects of antimycin on H-bond dynamics, we
also performed MD simulations on an antimycin-bound structure
of bacterial complex. Due to relatively weaker stability of antimycin
in our MD simulations, we restrained it to its crystallographic
position by harmonic restraints (see Table 2). We found that Ser
still makes H-bond to propionate (~20% ± 5% of total simulation
time). However, stable H-bonds to the carbonyl group of antimycin
are observed (~30% ± 9% occupancy) as long as it binds to the Q_i
site in a stable crystallographic arrangement (Fig. 3*H*). Interest-
ingly, the H-bond to antimycin from Ser occurs on an exclusive
basis such that H-bond to propionate ceases to exist. In WT case, a
weak H-bond to propionate was formed for ~15% ± 5% of the
simulation time; however, the Gly backbone was unable to form
the hydrogen bond with antimycin. Overall, the antimycin-bound
WT state resembles the H-bonding situation in the quinone-bound
WT state, but mutant explores an alternative H-bonding scenario
with antimycin. In addition, the "near/far" dynamics of antimycin-
bound cytochrome bc_1 are found to be similar to quinone-bound
simulations (both WT and mutant; Fig. 3*D*).

Table 2. Details of the MD simulation setups (B1-B4 bacterial bc_1 complex and M1-M2 mitochondrial bc_1 complex)

Setups	WT/mutant	Q_o/Q_i occupation	Replicas × time (ns)
B1	WT G48	Quinone/quinone	3 × 400 ns
B2	Mutant G48S	Quinone/quinone	3 × 400 ns
B3	WT G48	Quinone/antimycin*	3 × 300 ns
B4	Mutant G48S	Quinone/antimycin*	3 × 300 ns
M1	WT G48	Quinone/quinone	3 × 300 ns
M2	Mutant G48S	Quinone/quinone	3 × 300 ns

*Antimycin was restrained using harmonic spring to keep the head group in
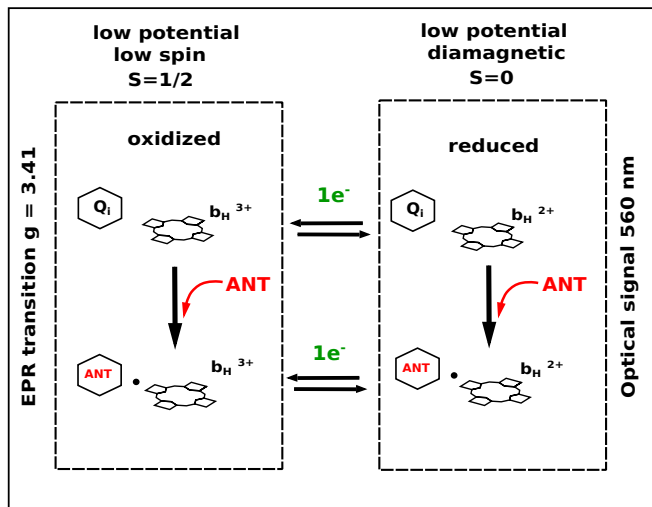place, using a force constant of 1,000 kJ · mol^{-1} · nm^{-2}.

Discussion

**Spectroscopic Studies and MD Simulations Implicate That H-Bonding
to Heme Propionate Affects the Redox Potential of Heme b_H.** Data
from our classical MD simulations reveal distinct differences
between WT and mutant cases and allow us to provide a mo-
lecular interpretation to experimental observations. We suggest that
the high potential heme b_{HH} signal is in part caused by the H-bond
to propionate from Gly or Ser. Indeed, our DFT calculations sup-
port that a Ser based H-bond may enhance electron affinity of heme
b_H. The higher proportion of heme b_{HH} in the mutant seen in ex-
periments is in excellent agreement with the higher occupancy of
the Ser-propionate H-bond compared to Gly. The heme b_{HL} can
therefore be assigned to the state where there is no hydrogen bond
between propionate and residue in concern. MD simulations also
suggest that a tightly bound antimycin can steal the hydrogen bond
with Ser to the propionate. This also agrees with the spectroscopic
data, which saw a loss of heme b_{HH} in the mutant with antimycin
present. Overall, our atomistic simulations and DFT calculations
provide a molecular picture on the origin of heme b_H signals ob-
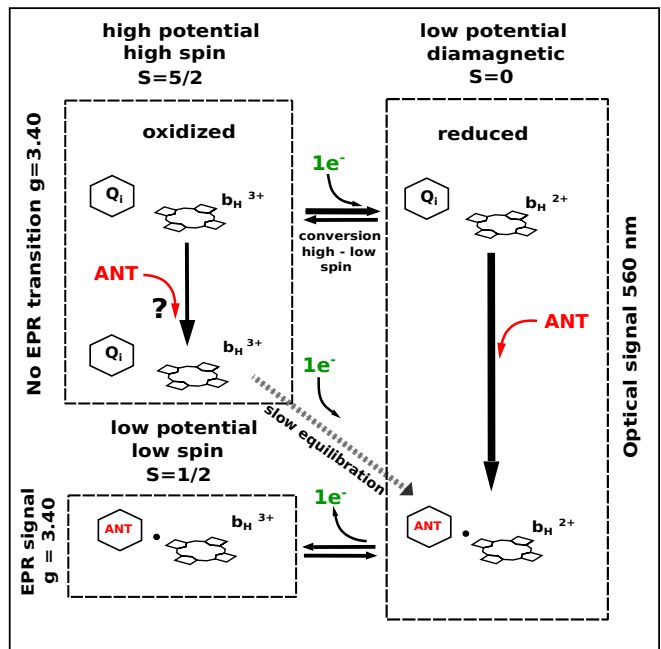served spectroscopically and discussed recently in ref. 21.

Model of Spin Conversion Observed for G48S Mutant. On the basis of
experimental data and supporting results from MD simulations,
the following molecular model of redox and magnetic states of
heme b_H in G48S can be proposed (Fig. 4). As this model considers
changes in the spin state of the heme, we first describe a well-
established case of the WT heme b_H (16). The fully oxidized
heme b_H has low spin (S = 1/2) and therefore can be observed in
CW EPR with characteristic transition g = 3.41. Optical spectrum of
oxidized heme in "α" region is broad with no absorption maximum
at 560 nm. Upon reduction, the spin state of heme b_H changes to
S = 0, which renders this heme invisible by EPR spectroscopy. The
reduction is associated with appearance of absorbance maximum at
560 nm in optical spectroscopy. Moreover, addition of Q_i site in-
hibitor, antimycin, at any redox state does not affect the spin state of
heme b_H (Fig. 4*A*).

In G48S, in contrast to WT, the heme b_H spin state depends
on its redox state. The fully oxidized heme b_H has high spin (S =
5/2), which results in the lack of the characteristic signal g = 3.40
in CW EPR. This high spin heme has a transition at g = 5.99,
which in membrane samples overlaps with other signals but can
be distinguished upon careful analysis of EPR redox titrations
(Fig. 2). The addition of antimycin to oxidized heme b_H in G48S
does not change its spin state, and consequently, the g = 3.40
transition is absent (Fig. 1*C*, red). The reduction of this heme
leads to the spin conversion from S = 5/2 to S = 0. Such form has
a clear maximum in optical spectrum (560 nm) and still no g =
3.40 transition. Only after subsequent oxidation does the g = 3.40
transition appear in the EPR spectrum of this mutant, meaning
that this heme achieves low spin state (S = 1/2).

Kuleta et al.
Hydrogen bonding rearrangement by a mitochondrial disease mutation in cytochrome
bc_1 perturbs heme b_H redox potential and spin state

Fig. 4. Model of the spin state conversion of heme b_H in G48S. (*A*) In WT, the oxidized heme b_H is low spin S = 1/2 (characteristic transition g_x = 3.41 in CW EPR spectroscopy; no maximum absorption at 560 nm in optical spectroscopy). Upon reduction, the heme b_H becomes diamagnetic and invisible in CW EPR (spin state S = 0) but can be observed on optical spectrum with maximum absorbance at 560 nm. Addition of antimycin does not affect the heme b_H spin state. (*B*) In G48S, the oxidized heme b_H is high spin S = 5/2 (no EPR signal at g = 3.40 and no maximum at 560 nm in optical spectroscopy). The addition of antimycin to G48S in the oxidized state does not change the spin state of heme or the appearance of EPR and optical signal. However, the prereduction of G48S sample with sodium ascorbate leads to spin conversion of heme b_H (from S = 5/2 to S = 0). Then, the reduced heme b_H is observed only in optical spectroscopy (no EPR signal). The addition of antimycin leads to lowering of heme b_H midpoint potential and in consequence oxidizing the sample prereduced with ascorbate (Fig. 1*B*), which then could be observed in EPR as the appearance of g_x = 3.40 transition (Fig. 2*B*).

Simulation analysis shows that in WT enzyme "near" arrangement is predominantly stabilized (Fig. 3*D*), which partly restricts the conformational flexibility of histidine ligand (*SI Appendix*, Fig. S4C). This is most likely due to the smaller volume of Gly residue that allows tighter packing in the vicinity of heme and its ligand. A glycine-induced cramped region would prevent flexibility of histidine ligand and thus help in stabilizing low spin state of heme. In contrast, population of "far" arrangement is much more enhanced in G48S mutant caused by the sidechain of serine. Such a change provides additional freedom to histidine ligand (His-111) of heme b_H to relax to higher spin states. Furthermore, due to the space created upon replacing Gly with Ser, hydration is enhanced in the vicinity of the heme propionate, which may also increase redox potential of the heme (see also ref. 27).

With this model, we can explain the ensemble of optical and EPR redox titrations (Figs. 1 *F* and *G* and 2) as well as the spectral changes in G48S relevant to the sequence of events described in Fig. 1 *B* and *C*. For the case shown in Fig. 1*B*, the addition of antimycin to ascorbate-reduced sample lowers the heme b_H midpoint potential, resulting in its oxidation. This makes the heme b_H detectable in EPR as g = 3.40 transition (red spectrum), which could not be observed before the spin conversion (black spectrum). The case shown in Fig. 1*C* can be explained with two possible scenarios. In the first one, antimycin does not bind to oxidized high spin heme b_H until this heme is reduced by ascorbate. After reduction, the heme undergoes conversion to low spin and then antimycin binds, lowering its E_m, which results in oxidation of this heme. In the second scenario, antimycin binds to oxidized high spin heme b_H and lowers its E_m. Addition of ascorbate induces spin conversion of this heme but does not reduce it. Because both of these scenarios would result in the appearance of EPR g = 3.40 transition, typical of oxidized low spin heme (as seen by comparison

of the red vs. green spectrum in Fig. 1*C*), it cannot be decided whether antimycin binds to the oxidized high spin or to reduced low spin heme b_H.

The proposed model provides a detailed understanding of the molecular effects of exercise intolerance-related homologous Gly to Ser mutation in cytochrome *b* of human mitochondrial complex III. Given the light-induced electron transfer competence of G48S substitution (Table 1), one would expect that the overall electron flux is not largely altered in the mutant cells. Nevertheless, the heme *b* reoxidation and the Q_i site reverse reaction are slowed by 4- and 10-fold, respectively, in the mutant in comparison to the WT. The spin conversion in G48S might be at the root of these perturbed kinetic effects. MD simulations indicate that H-bonding patterns of heme b_H propionate in bacterial and mitochondrial Gly to Ser mutants are similar. Given the overall similarities, also at the sequence level, it follows that heme b_H in mitochondrial mutant might also undergo spin conversion, which, in analogy to the bacterial system, might introduce limitations to the rate of electron transfer. One may expect such limitations to have a larger impact on the cells especially under stress or the conditions of increased energetic demands (high proton motive force, for instance). Another possible molecular effect that contributes to the exercise intolerance is the decreased stability of the mutated cytochrome bc_1 complex implicated from this study and also from the studies with yeast cytochrome bc_1 (8). We note that overall effects of this Gly to Ser mutation are expected to be subtle, as reported in other cases (see example in ref. 28); otherwise, the mutation would have been lethal to the cells.

The Dual Effect of the Strength of H-Bond to Heme Propionate. Considering mutational studies on other redox-active enzymes, it is reasonable to expect that the alteration of H-bonds to heme

Kuleta et al.
Hydrogen bonding rearrangement by a mitochondrial disease mutation in cytochrome bc_1
perturbs heme b_H redox potential and spin state

PNAS | 7 of 10
https://doi.org/10.1073/pnas.2026169118

propionates modulates the redox potential of the heme (see examples in refs. 29–31). In view of our data, the H-bond to heme propionate from the amino acid at position 48 appears to have a dual effect. On one hand, change of H-bond donor from backbone of Gly to sidechain of Ser leads to its stabilization and an increase in the redox potential of the heme. On the other hand, it appears to perturb interactions between Fe ion and axial histidine ligands, which leads to a reversible spin conversion of the oxidized Fe ion from $S = 1/2$ to $S = 5/2$. However, the latter effect should be regarded as undesired for hemes that are part of electron transfer chains. The spin state of those hemes is typically $S = 0$ and $S = 1/2$ for reduced and oxidized state, respectively, and spin conversion at a given redox state is avoided. This is because such a conversion can potentially reduce the electron transfer rate between any given heme and its redox partners, as implicated from kinetic impediments between heme b_H and the occupant of the Q_i site in G48S. In view of this dual effect, it can be suggested that the strength of the H-bond in the native protein was optimized to secure both the high potential and the low spin and diamagnetic form of heme in the oxidized and reduced state, respectively. We anticipate that similar design principles might apply for other native heme proteins and, possibly, be exploited when designing artificial heme protein maquettes of specific redox properties (32, 33).

Materials and Methods

Genetic Modifications. *R. capsulatus* cells containing glycine to serine substitution at position 48 in cytochrome *b* subunit were obtained using a genetic system described in ref. 34. G48S mutation was introduced in the *petB* gene coding for cytochrome *b* gene using QuikChange site-directed mutagenesis system (Stratagene) and the following PCR primers (the mutated nucleotides are marked in bold in the underlined triplet): G48S_FWD, 5′–GAACTGGTGGTGGATCTGG**TC**GATCGTCCTTGCCTTC-ACG–3′, and G48S_REV, 5′–GTGAAGGCAAGGACGAT**CGA**CCAGATCCACCACCA-GTTC–3′. As a template DNA, the pPET1 plasmid containing WT *petABC* operon was used. The *Bst*XI-*Asu*II fragment of the operon containing the desired mutation, and no other mutations, was inserted into pMTS1 vector and introduced into MT-RBC1 *R. capsulatus* strain using triparental crossing (34). The presence of introduced mutation was confirmed by sequence analysis of *petB* gene on plasmid isolated from mutated *R. capsulatus* strain.

Cell Growth and Preparation of Chromatophores. *R. capsulatus* bacteria were grown under semiaerobic conditions on mineral-peptone-yeast extract (MPYE) medium. The tests of bc_1-dependent growth under photosynthetic conditions were performed on MPYE-agar plates containing 100 μL bacteria diluted from overnight cultures to $OD_{600} = 0.1$, incubated in anaerobic jars (GasPak System, BD) at 30 °C under continuous light. Chromatophore membranes were prepared from 10 L liquid cultures with a French pressure cell at 16,000 psi followed by separation on ultracentrifuge according to the procedure described previously (35). After homogenization chromatophores were suspended in 50 mM 3-(N-Morpholino)propanesulfonic acid (MOPS) buffer (pH 7.0, 100 mM KCl, 1 mM EDTA) and stored at 4 °C.

Light-Activated Redox Reactions of Hemes. Double-wavelength time-resolved spectrophotometer (36) was used to measure the kinetics of electron transfer through the heme cofactors of cytochrome bc_1. Measurements were performed according to refs. 37 and 38 using chromatophores suspended in MOPS buffer poised at redox potential 100 mV or in 50 mM Tris buffer (pH 9.0, 100 mM KCl, 1 mM EDTA) poised at 250 mV. Sodium dithionite or ferricyanide were used to adjust the ambient redox potential (E_h) of chromatophore suspensions. The samples were sustained under anaerobic conditions in the presence of 3.5 μM valinomycin and the following redox mediators: 7 μM 2,3,5,6-tetramethyl-1,4-phenylenediamine, 1 μM phenazine methosulfate, 1 μM phenazine ethosulfate, 5.5 μM 1,2-naphthoquinone, and 5.5 μM 2-hydroxy-1,4-naphthoquinone. Transient kinetics of hemes *b* were monitored at 560 to 570 nm after activation by single saturating light pulse (~10 μs). The rates of flash-induced electron transfer reactions were determined from single exponential function fitted to kinetic traces of heme b_H reduction (in the presence of antimycin), b_H reoxidation (without inhibitors), and heme b_H reduction from

reverse reaction (in the presence of myxothiazol). Inhibitors were used at final concentration of 7 μM.

Optical and EPR Spectroscopy. The optical absorption spectra of membrane chromatophores were performed on a Shimadzu UV-2450 spectrophotometer. The samples were suspended in MOPS buffer and measured in the wavelength range of 500 to 600 nm. The ferricyanide was added to oxidize the samples, whereas for reduction, the sodium ascorbate and sodium dithionite were used (to reduce high- and low-potential b-type hemes, respectively). The spectra were recorded right after oxidation and after each step of reduction with ascorbate and dithionite at room temperature. CW EPR spectra of hemes were measured at X band frequency (9.4 GHz) using membrane chromatophores. Samples of WT and mutant were prepared in MOPS buffer. Samples were quickly frozen in liquid nitrogen and measured at 20 K. All EPR measurements were carried on a Bruker Elexsys E580 spectrometer using a SHQEOS11 resonator combined with ESR900 Oxford Instruments cryostat unit and the following parameters: resonance frequency, 9.39 GHz; microwave power, 1.9 mW; and modulation amplitude, 15 G.

Redox Potentiometry. Redox midpoint potentials of hemes *b* were determined by dark equilibrium redox titrations on chromatophores according to the method described previously (39). Chromatophores were suspended in MOPS buffer and sustained under anaerobic conditions in the presence of redox mediators: 100 μM tetrachlorohydroquinone, 100 μM 2,3,5,6-tetramethyl phenylenediamine, 100 μM 1,2-naphtoquinone-4-sulfonate, 100 μM 1,2-naphtoquinone, 50 μM phenazine methosulfate, 50 μM phenazine ethosulfate, 100 μM duroquinone, 30 μM indigotrisulfonate, 100 μM 2-hydroxy-1,4-napthoquinone, 100 μM anthroquinone-2-sulfonate, and 100 μM benzyl viologen. Dithionite and ferricyanide were used to adjust ambient redox potential. During the EPR redox titration at certain ambient potential (E_h), the small aliquots of the sample (~200 μL) were transferred to argon-flushed EPR tubes, quickly frozen in liquid nitrogen, and measured using parameters described above. The E_{m7} values of hemes *b* were determined by fitting the amplitudes of appropriate EPR g transitions to the Nernst equation for a one-electron couple with estimated uncertainties of approximately ±15 mV.

Computational Methods. To complement our experiments on cytochrome bc_1 complex from photosynthetic bacterium *R. capsulatus*, we performed fully atomistic MD simulations on the 3.5 Å resolution structure of the same complex (PDB ID: 1ZRT) (25). The protein was placed in a POPC lipid bilayer using the CHARMM-GUI online tool (40). An oxidized quinone (Q10) molecule was modeled at both the Q_i and Q_o sites in each monomer, and the [2Fe-2S] cluster and heme c_1 were modeled in the reduced state, while the heme b_L and heme b_H were kept oxidized. Simulations with antimycin occupying the Q_i site were also performed using the same crystal structure. Both WT and mutant (G48S) systems were constructed and simulated. Since the studied mutant is associated with mitochondrial dysfunction, we also performed MD simulations on the high resolution (1.9 Å) structure of cytochrome bc_1 from yeast *S. cerevisiae* (PDB ID: 3CX5) (26) modeled in hybrid lipid bilayer consisting of 50% POPC, 35% POPE, and 15% cardiolipin. In both bacterial and mitochondrial model systems, all amino acids were kept in their standard protonation states, that is, Lys, Arg, Glu, and Asp in their charged states and all His residues in neutral state with Nδ protonated. The systems were solvated with TIP3P water molecules and 0.1 M NaCl salt concentration, resulting in a final system size of ~285,000 atoms for bacterial systems (setups B1 to B4 in Table 2; see also *SI Appendix*, Fig. S1C) and ~580,000 atoms for mitochondrial systems (setups M1 and M2 in Table 2). CHARMM forcefield (41–43) was used for protein, lipids, water, and ions together with the force field parameters of antimycin obtained from CHARMM-GUI (40). The parameters of Q10 and metal centers were obtained from refs. 44 and 45, respectively. The MD procedure consisted of an initial energy minimization with constraints on heavy atoms, followed by 500 ps NVT (canonical ensemble, constant number of particles N, volume V and temperature T) and 1 ns NPT (isothermal-isobaric ensemble, constant number of particles N, pressure P and temperature T) equilibration steps, with constraints being gradually reduced throughout the equilibration. All simulations were performed with GROMACS 2016.4 and 2020.3 software (46) at 310 K and 1 atm pressure, with the temperature and pressure being controlled by the Nose-Hoover thermostat (47, 48) and Parrinello-Rahman barostat (49, 50), respectively. The electrostatic interactions were computed using the PME method (51) as implemented, and the LINCS algorithm (52) was used to achieve a step-size of 2 fs. The total production simulation time was ~6 μs, and Table 2 shows details of the systems and simulation time lengths.

DFT calculations were performed to study the redox behavior of heme b_H in WT and mutant states. Snapshots ($n = 3$) from MD simulations of bacterial complex were used to construct the WT and mutant cluster models for DFT

calculations. Models comprised heme b_H, its histidine ligands, and surrounding residues, totaling ~200 atoms (*SI Appendix*, Fig. S1D). The total charge of the system in reduced and oxidized state was −1 and 0, respectively, and spin states considered were S = 0 and 1/2, respectively. Similar WT and mutant cluster models were also constructed using the high-resolution structure of yeast cytochrome bc_1. DFT-based geometry optimizations were performed with the BP86 functional (53, 54) and def2-SVP basis set on all atoms other than Fe, where the larger def2-TZVP (55) basis set was used. All protein backbone atoms were removed apart from the C_β atoms, which were fixed during geometry optimizations (*SI Appendix*, Fig. S1D). Dispersion corrections were applied (56) with Becke-Johnson damping (57). Single point calculations were then performed on the optimized structures using the def2-TZVP (55) basis set on all atoms, and three different density functionals, B3LYP (54, 58, 59), TPSS, and TPSSh (60), were used. The COSMO model (61) was employed to describe a dielectric constant of 4, mimicking the protein environment. All DFT calculations were performed using TURBOMOLE 7.3 software (62).

1. E. A. Berry, F. A. Walker, Bis-histidine-coordinated hemes in four-helix bundles: How the geometry of the bundle controls the axial imidazole plane orientations in transmembrane cytochromes of mitochondrial complexes II and III and related proteins. *J. Biol. Inorg. Chem.* **13**, 481–498 (2008).
2. G. Battistuzzi, M. Borsari, J. A. Cowan, A. Ranieri, M. Sola, Control of cytochrome c redox potential: Axial ligation and protein environment effects. *J. Am. Chem. Soc.* **124**, 5315–5324 (2002).
3. J. Mao, K. Hauser, M. R. Gunner, How cytochromes with different folds control heme redox potentials. *Biochemistry* **42**, 9829–9840 (2003).
4. G. R. Moore, G. W. Pettigrew, *Cytochromes c: Evolutionary, Structural and Physicochemical Aspects* (Springer-Verlag, Berlin, Germany, 1990).
5. H. B. Gray, J. R. Winkler, Electron flow through metalloproteins. *Biochim. Biophys. Acta* **1797**, 1563–1572 (2010).
6. H. B. Gray, J. R. Winkler, Electron transfer in proteins. *Annu. Rev. Biochem.* **65**, 537–561 (1996).
7. J. S. Kretchmer et al., Fluctuating hydrogen-bond networks govern anomalous electron transfer kinetics in a blue copper protein. *Proc. Natl. Acad. Sci. U.S.A.* **115**, 6129–6134 (2018).
8. N. Fisher et al., Human disease-related mutations in cytochrome b studied in yeast. *J. Biol. Chem.* **279**, 12951–12958 (2004).
9. R. Ekiert, A. Borek, P. Kuleta, J. Czernek, A. Osyczka, Mitochondrial disease-related mutations at the cytochrome b-iron-sulfur protein (ISP) interface: Molecular effects on the large-scale motion of ISP and superoxide generation studied in *Rhodobacter capsulatus* cytochrome bc_1. *Biochim. Biophys. Acta* **1857**, 1102–1110 (2016).
10. A. L. Andreu et al., Exercise intolerance due to mutations in the cytochrome b gene of mitochondrial DNA. *N. Engl. J. Med.* **341**, 1037–1044 (1999).
11. T. Tron, M. Crimi, A. M. Colson, M. Degli Esposti, Structure/function relationships in mitochondrial cytochrome b revealed by the kinetic and circular dichroic properties of two yeast inhibitor-resistant mutants. *Eur. J. Biochem.* **199**, 753–760 (1991).
12. M. D. Esposti et al., Mitochondrial cytochrome b: Evolution and structure of the protein. *Biochim. Biophys. Acta* **1143**, 243–271 (1993).
13. C.-H. Yun, Z. Wang, A. R. Crofts, R. B. Gennis, Examination of the functional roles of 5 highly conserved residues in the cytochrome b subunit of the bc_1 complex of *Rhodobacter sphaeroides*. *J. Biol. Chem.* **267**, 5901–5909 (1992).
14. J. Y. Coppée et al., Analysis of revertants from respiratory deficient mutants within the center N of cytochrome b in *Saccharomyces cerevisiae*. *FEBS Lett.* **339**, 1–6 (1994).
15. B. Meunier, N. Fisher, S. Ransac, J.-P. Mazat, G. Brasseur, Respiratory complex III dysfunction in humans and the use of yeast as a model organism to study mitochondrial myopathy and associated diseases. *Biochim. Biophys. Acta* **1827**, 1346–1361 (2013).
16. J. C. Salerno, Cytochrome electron spin resonance line shapes, ligand fields, and components stoichiometry in ubiquinol-cytochrome c oxidoreductase. *J. Biol. Chem.* **259**, 2331–2336 (1984).
17. D. E. Robertson et al., Hydroubiquinone-cytochrome c_2 oxidoreductase from *Rhodobacter capsulatus*: Definition of a minimal, functional isolated preparation. *Biochemistry* **32**, 1310–1317 (1993).
18. S. Pintscher et al., Tuning of hemes b equilibrium redox potential is not required for cross-membrane electron transfer. *J. Biol. Chem.* **291**, 6872–6881 (2016).
19. E. G. Glaser, S. W. Meinhardt, A. R. Crofts, Reduction of cytochrome b-561 through the antimycin-sensitive site of the ubiquinol-cytochrome c_2 oxidoreductase complex of *Rhodopseudomonas sphaeroides*. *FEBS Lett.* **178**, 336–342 (1984).
20. K. A. Gray, P. L. Dutton, F. Daldal, Requirement of histidine 217 for ubiquinone reductase activity (Q_i site) in the cytochrome bc_1 complex. *Biochemistry* **33**, 723–733 (1994).
21. S. Pintscher, A. Wójcik-Augustyn, M. Sarewicz, A. Osyczka, Charge polarization imposed by the binding site facilitates enzymatic redox reactions of quinone. *Biochim. Biophys. Acta Bioenerg.* **1861**, 148216 (2020).
22. M. G. Finnegan et al., Axial heme ligation in the cytochrome bc_1 complexes of mitochondrial and photosynthetic membranes. A near-infrared magnetic circular dichroism and electron paramagnetic resonance study. *Biochim. Biophys. Acta* **1274**, 9–20 (1996).
23. G. Zoppellaro et al., Review: Studies of ferric heme proteins with highly anisotropic/highly axial low spin (S = 1/2) electron paramagnetic resonance signals with bishistidine and histidine-methionine axial iron coordination. *Biopolymers* **91**, 1064–1082 (2009).
24. J. Peisach, W. E. Blumberg, S. Ogawa, E. A. Rachmilewitz, R. Oltzik, The effects of protein conformation on the heme symmetry in high spin ferric heme proteins as studied by electron paramagnetic resonance. *J. Biol. Chem.* **246**, 3342–3355 (1971).
25. E. A. Berry et al., X-ray structure of *Rhodobacter capsulatus* cytochrome bc_1: Comparison with its mitochondrial and chloroplast counterparts. *Photosynth. Res.* **81**, 251–275 (2004).
26. S. R. N. Solmaz, C. Hunte, Structure of complex III with bound cytochrome c in reduced state and definition of a minimal core interface for electron transfer. *J. Biol. Chem.* **283**, 17542–17549 (2008).
27. C. A. Bortolotti et al., The reversible opening of water channels in cytochrome c modulates the heme iron reduction potential. *J. Am. Chem. Soc.* **134**, 13670–13678 (2012).
28. J. Purhonen et al., A spontaneous mitonuclear epistasis converging on Rieske Fe-S protein exacerbates complex III deficiency in mice. *Nat. Commun.* **11**, 322 (2020).
29. H. J. Lee, L. Öjemyr, A. Vakkasoglu, P. Brzezinski, R. B. Gennis, Properties of Arg481 mutants of the aa_3-type cytochrome c oxidase from *Rhodobacter sphaeroides* suggest that neither R481 nor the nearby D-propionate of heme a_3 is likely to be the proton loading site of the proton pump. *Biochemistry* **48**, 7123–7131 (2009).
30. D. A. Mills et al., An arginine to lysine mutation in the vicinity of the heme propionates affects the redox potentials of the hemes and associated electron and proton transfer in cytochrome c oxidase. *Biochemistry* **44**, 10457–10465 (2005).
31. H. B. Gray, J. R. Winkler, Long-range electron transfer. *Proc. Natl. Acad. Sci. U.S.A.* **102**, 3534–3539 (2005).
32. D. E. Robertson et al., Design and synthesis of multi-haem proteins. *Nature* **368**, 425–432 (1994).
33. B. R. Lichtenstein et al., Engineering oxidoreductases: Maquette proteins designed from scratch. *Biochem. Soc. Trans.* **40**, 561–566 (2012).
34. E. Atta-Asafo-Adjei, F. Daldal, Size of the amino acid side chain at position 158 of cytochrome b is critical for an active cytochrome bc_1 complex and for photosynthetic growth of *Rhodobacter capsulatus*. *Proc. Natl. Acad. Sci. U.S.A.* **88**, 492–496 (1991).
35. M. B. Valkova-Valchanova, A. S. Saribaş, B. R. Gibney, P. L. Dutton, F. Daldal, Isolation and characterization of a two-subunit cytochrome b-c_1 subcomplex from *Rhodobacter capsulatus* and reconstitution of its ubihydroquinone oxidation (Q_o) site with purified Fe-S protein subunit. *Biochemistry* **37**, 16242–16251 (1998).
36. E. Cieluch, K. Pietryga, M. Sarewicz, A. Osyczka, Visualizing changes in electron distribution in coupled proteins of cytochrome bc_1 by modifying barrier for electron transfer between the FeS cluster and heme c_1. *Biochim. Biophys. Acta* **1797**, 296–303 (2010).
37. D. E. Robertson et al., Discrete catalytic sites for quinone in the ubiquinol-cytochrome c_2 oxidoreductase of *Rhodopseudomonas capsulata*. Evidence from a mutant defective in ubiquinol oxidation. *J. Biol. Chem.* **261**, 584–591 (1986).
38. R. E. Sharp et al., Ubiquinone binding capacity of the *Rhodobacter capsulatus* cytochrome bc_1 complex: Effect of diphenylamine, a weak binding Q_O site inhibitor. *Biochemistry* **38**, 3440–3446 (1999).
39. P. L. Dutton, Redox potentiometry: Determination of midpoint potentials of oxidation-reduction components of biological electron-transfer systems. *Methods Enzymol.* **54**, 411–435 (1978).
40. S. Jo, T. Kim, V. G. Iyer, W. Im, CHARMM-GUI: A web-based graphical user interface for CHARMM. *J. Comput. Chem.* **29**, 1859–1865 (2008).
41. A. D. MacKerell et al., All-atom empirical potential for molecular modeling and dynamics studies of proteins. *J. Phys. Chem. B* **102**, 3586–3616 (1998).
42. A. D. Mackerell Jr, M. Feig, C. L. Brooks III, Extending the treatment of backbone energetics in protein force fields: Limitations of gas-phase quantum mechanics in reproducing protein conformational distributions in molecular dynamics simulations. *J. Comput. Chem.* **25**, 1400–1415 (2004).
43. J. B. Klauda et al., Update of the CHARMM all-atom additive force field for lipids: Validation on six lipid types. *J. Phys. Chem. B* **114**, 7830–7843 (2010).
44. V. V. Galassi, G. M. Arantes, Partition, orientation and mobility of ubiquinones in a lipid bilayer. *Biochim. Biophys. Acta* **1847**, 1560–1573 (2015).
45. K. Kaszuba et al., Parameterization of the prosthetic redox centers of the bacterial cytochrome bc_1 complex for atomistic molecular dynamics simulations. *Theor. Chem. Acc.* **132**, 1370–1383 (2013).
46. M. J. Abraham et al., Gromacs: High performance molecular simulations through multi-level parallelism from laptops to supercomputers. *SoftwareX* **1–2**, 19–25 (2015).
47. S. Nosé, A unified formulation of the constant temperature molecular dynamics methods. *J. Chem. Phys.* **81**, 511–519 (1984).

Kuleta et al.
Hydrogen bonding rearrangement by a mitochondrial disease mutation in cytochrome bc_1 perturbs heme b_H redox potential and spin state

PNAS | 9 of 10
https://doi.org/10.1073/pnas.2026169118

48. W. G. Hoover, Canonical dynamics: Equilibrium phase-space distributions. *Phys. Rev. A Gen. Phys.* **31**, 1695–1697 (1985).

49. M. Parrinello, A. Rahman, Crystal structure and pair potentials: A molecular-dynamics study. *Phys. Rev. Lett.* **45**, 1196–1199 (1980).

50. M. Parrinello, A. Rahman, Polymorphic transitions in single crystals: A new molecular dynamics method. *J. Appl. Phys.* **52**, 7182–7190 (1981).

51. T. Darden, D. York, L. Pedersen, Particle mesh Ewald: An Nlog(N) method for Ewald sums in large systems. *J. Chem. Phys.* **98**, 10089–10092 (1993).

52. B. Hess, H. Bekker, H. J. C. Berendsen, J. G. E. M. Fraaije, LINCS: A Linear Constraint Solver for molecular simulations. *J. Comput. Chem.* **18**, 1463–1472 (1997).

53. J. P. Perdew, Density-functional approximation for the correlation energy of the in-homogeneous electron gas. *Phys. Rev. B Condens. Matter* **33**, 8822–8824 (1986).

54. A. D. Becke, Density-functional exchange-energy approximation with correct asymptotic behavior. *Phys. Rev. A Gen. Phys.* **38**, 3098–3100 (1988).

55. F. Weigend, R. Ahlrichs, Balanced basis sets of split valence, triple zeta valence and quadruple zeta valence quality for H to Rn: Design and assessment of accuracy. *Phys. Chem. Chem. Phys.* **7**, 3297–3305 (2005).

56. S. Grimme, J. Antony, S. Ehrlich, H. Krieg, A consistent and accurate *ab initio* parametrization of density functional dispersion correction (DFT-D) for the 94 elements H-Pu. *J. Chem. Phys.* **132**, 154104 (2010).

57. S. Grimme, S. Ehrlich, L. Goerigk, Effect of the damping function in dispersion corrected density functional theory. *J. Comput. Chem.* **32**, 1456–1465 (2011).

58. A. D. Becke, Density-functional thermochemistry. III. The role of exact exchange. *J. Chem. Phys.* **98**, 5648–5652 (1993).

59. C. Lee, W. Yang, R. G. Parr, Development of the Colle-Salvetti correlation-energy formula into a functional of the electron density. *Phys. Rev. B Condens. Matter* **37**, 785–789 (1988).

60. J. Tao, J. P. Perdew, V. N. Staroverov, G. E. Scuseria, Climbing the density functional ladder: Nonempirical meta-generalized gradient approximation designed for molecules and solids. *Phys. Rev. Lett.* **91**, 146401 (2003).

61. A. Klamt, G. Schüürmann, COSMO: A new approach to dielectric screening in solvents with explicit expressions for the screening energy and its gradient. *J. Chem. Soc., Perkin Trans.* 2799–805 (1993).

62. S. G. Balasubramani *et al.*, TURBOMOLE: Modular program suite for *ab initio* quantum-chemical and condensed-matter simulations. *J. Chem. Phys.* **152**, 184107 (2020).